Composites: Part A 165 (2023) 107323

Contents lists available at ScienceDirect

Composites Part A

journal homepage: www.elsevier.com/locate/compositesa

A hyperelastic material model considering biaxial coupling of tension–compression and shear for the forming simulation of woven fabrics

Florian Schäfer [a,*], Henrik O. Werner [a,b], Frank Henning [a,c], Luise Kärger [a,*]

[a] Karlsruhe Institute of Technology (KIT), Institute for Vehicle System Technology, Division Lightweight Design, Rintheimer Querallee 2, 76131 Karlsruhe, Germany
[b] Karlsruhe Institute of Technology (KIT), Institute for Applied Materials (IAM), Engelbert-Arnold-Straße 4, 76131 Karlsruhe, Germany
[c] Fraunhofer Institute for Chemical Technology (ICT), Polymer Engineering Department, Joseph-von-Fraunhofer-Str. 7, 76327 Pfinztal, Germany

ARTICLE INFO

Keywords:
Fabrics/Textiles
Process modeling
Hyperelastic

ABSTRACT

In the past decades, numerous material models have been developed to describe the forming behavior of fabrics, allowing for modeling of complex forming processes. Especially under constrained forming conditions, distinct multiaxial stress states can occur, which need to be captured by macroscopic material models. In this paper, a nonlinear hyperelastic constitutive model is presented and implemented in an Abaqus/Explicit user subroutine Vumat, considering biaxial coupling and normal-shear coupling of the interwoven fiber bundles in a woven fabric. The couplings are formulated for positive and negative normal strains. Exemplary forming studies on the generic double dome geometry are performed to investigate the influence of the couplings on the forming result. The results show that the biaxial coupling should be considered under highly constrained boundary conditions in thickness direction. The normal-shear coupling affects the forming behavior only under very high draping angles and appears to be of less relevance in these conditions.

1. Introduction

In recent years, the issues of sustainability and climate protection have emerged as increasingly important to society. Because carbon dioxide emissions in the use-phase of a vehicle are proportional to its mass, systematic lightweight design is key to improve the environmental balance, independent of future drive technologies [1]. In addition to established light metals, composite structures, such as fiber-reinforced polymers, are becoming increasingly important for achieving weight reductions. Woven fabrics are often used as reinforcement due to their ease in production and handling compared to non-crimped fabrics. To design complex geometric structures and their associated manufacturing processes, a precise understanding of the material behavior is necessary. Because experimental trials are expensive in terms of time and resources, numerical calculations are often used [2]. The virtual process chain models the entire manufacturing process by means of numerical methods [3,4]. The first step is, to describe the material behavior of the fabric during forming, when the two-dimensional textile product is displaced into a three-dimensional geometry. Material modeling requires a deep understanding of the deformation mechanisms in fabrics.

Woven fabrics are mostly plane structures consisting of interwoven fiber bundles. At the micro-scale, several thousand single fibers form bundles called rovings that are often assumed to be homogeneous at the meso-scale. At the macro-level, the fabric is assumed to be a homogeneous solid, and no single rovings are considered [5]. The most common forms of fabric consist of interwoven rovings in two directions. Fig. 1 shows the schematic structure of a plain weave fabric. Due to the interwoven structure, interactions occur between rovings at the meso-level, leading to geometrical changes and resulting in a biaxially coupled, nonlinear material behavior at the macro-level. Many research groups offer detailed discussions on the deformation mechanisms at the meso-scale and the resulting macroscopic material behavior [5–13]. Comprehensive reviews are published in [14,15]. In free draping, compressive stresses lead to extensive wrinkling, as the bending stiffness of fabrics is low compared to their tensile stiffness. Therefore, membrane and bending behavior of fabrics should be modeled decoupled [12,16–22], as shown in Fig. 1. Wrinkling can be suppressed by blank holders, grippers or, in case of fiber-metal-laminates (FML), by encasing metal layers. Hence, combined stress zones may occur during forming. Werner et al. [23,24] numerically investigated the influence of the not infiltrated fabric material parameters on the forming result during FML forming and concluded, that the bending behavior in highly constrained conditions in thickness direction is less important compared to the membrane behavior. Therefore, the membrane behavior influences the forming result more significantly, than in free or close to free draping

* Corresponding authors.
E-mail addresses: florian.schaefer93@t-online.de (F. Schäfer), luise.kaerger@kit.edu (L. Kärger).

https://doi.org/10.1016/j.compositesa.2022.107323
Received 6 February 2022; Received in revised form 31 October 2022; Accepted 13 November 2022
Available online 21 November 2022

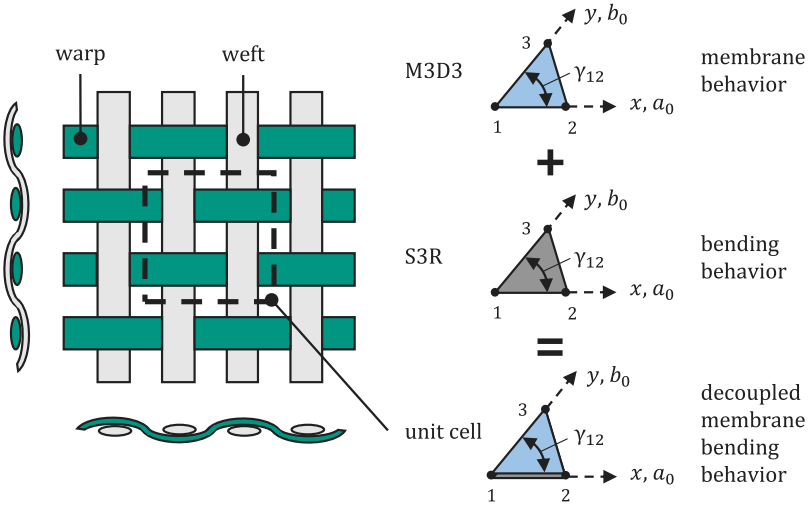

Fig. 1. Structure of a plain weave fabric including cross-sections (left) and highlighted unit cell for decoupled material discretization in forming simulation (right) according to [19,22].

conditions. To model the material behavior of fabrics in highly constrained conditions in thickness direction, Werner et al. [14] suggest incorporating biaxial coupling, normal-shear coupling and in-plane compression behavior.

For application in numerical simulations of fabrics, modeling techniques on different levels are feasible. The most common approaches are models at the mesoscopic or macroscopic levels. In meso-scale-models, interactions between rovings are considered intrinsically, but elaborate and detailed modeling of the weave architecture is necessary. In macro-scale-models, however, the whole fabric is assumed to be a continuum. Here, the complex material behavior has to be embedded in the constitutive equations. As a consequence, established material models of monolithic materials cannot be used to describe the behavior of fabrics adequately. Thus, tailored material models need to be developed. A pivotal selection criterion is the model's efficiency. To achieve acceptable computation times for numerical calculations at the component level, macro-scale-models are particularly suitable [3,11,12,25–30].

The two most common approaches are models based on Cauchy-elasticity and hyperelasticity [14,15]. In Cauchy-elasticity, stresses are direct functions of the strains. This relationship is defined via the stiffness. When modeling the material behavior of fabrics, material properties need to be formulated with respect to the roving orientations and as fabrics are prone to large shear deformation, an elaborate nonorthogonal formulation of the constitutive equations is necessary [31]. Several research groups make use of this approach [32,33], some of them considering biaxial tension coupling [34] and tension–shear coupling [35]. In hyperelasticity, however, an integral representation of the stress–strain relationship is used, and the stresses can be calculated from the strain energy density by differentiation with respect to a strain measure. The strain energy density is a scalar function representing an elastic potential and is thus a measure of the strain energy stored in a deformed body. It can be additively decomposed into several components attributed to different deformation mechanisms. Depending on the choice of the stress measure and its corresponding strain measure, a formulation of the constitutive equations in the initial configuration can be found. To guarantee independency from the chosen basis system, making use of invariants is recommended [29]. This approach is pursued in several publications [36,37] and permits the possibility to incorporate the relevant coupling phenomenon [38–40]. Also, an extension to negative strains is viable.

For the present requirements, the authors suggest a hyperelastic, invariant-based material model based on the work published by [29, 36–40]. A new hyperelastic material model is presented, considering biaxial coupling, normal-shear coupling for positive and negative strains, as well as in-plane compression behavior. At first, the principles of hyperelastic material modeling are summarized, and then a new model is deduced to describe the material behavior. Subsequently, the material model is fitted to data from literature and after numerical verification, exemplary numerical calculations are performed for tensile and bias-extension test specimens and for a double-dome geometry according to Sargent et al. [41]. The results are analyzed and compared to similar calculations that make use of the Abaqus/Explicit built-in Fabric-model. Finally, the material model is discussed with regard to its scope, potential enhancements and a validation strategy.

2. Methods

2.1. Fundamentals of hyperelasticity

In hyperelasticity, an integral representation of the stress–strain relationship is used, in which stresses and strains are linked via the strain energy density W according to

$$\boldsymbol{\sigma} = \frac{\partial W}{\partial \boldsymbol{\varepsilon}}. \tag{1}$$

For materials with direction-dependent properties, it is beneficial to use a material model that allows to describe the material behavior in the initial configuration. The second Piola–Kirchhoff stresses (PKS) $\boldsymbol{S}$ can be expressed via

$$\boldsymbol{S} = 2\frac{\partial W(\boldsymbol{C})}{\partial \boldsymbol{C}} \tag{2}$$

depending on the right Cauchy–Green (RCG) tensor $\boldsymbol{C}$, which can be deduced from the deformation gradient $\boldsymbol{F}$ by means of the polar composition

$$\boldsymbol{C} = \boldsymbol{F}^{\top}\boldsymbol{F} = (\boldsymbol{R}\boldsymbol{U})^{\top}\,\boldsymbol{R}\boldsymbol{U} = \boldsymbol{U}^{\top}\boldsymbol{R}^{\top}\,\boldsymbol{R}\boldsymbol{U} = \boldsymbol{U}^{2}. \tag{3}$$

The tensors $\boldsymbol{R}$ and $\boldsymbol{U}$ are the proper orthogonal rotation tensor and the right stretch tensor, respectively [42]. Fig. 2 depicts the polar decomposition of the deformation gradient and shows how the initial fiber orientations $\boldsymbol{a}_0$ and $\boldsymbol{b}_0$ transform. The second PKS can be transformed into Cauchy-stresses via

$$\boldsymbol{\sigma} = \frac{1}{J}\,\boldsymbol{F}\cdot\boldsymbol{S}\cdot\boldsymbol{F}^{\top}, \tag{4}$$

where J is the Jacobian of $\boldsymbol{F}$ [43].

To avoid basis-dependency, invariants are used when formulating the constitutive equations. Based on the RCG tensor and the initial fiber

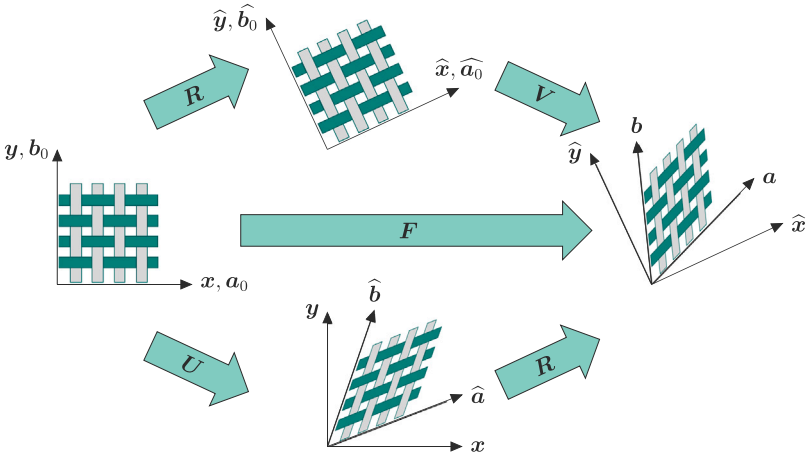

Fig. 2. Polar decomposition of the deformation gradient applied to a fabric structure.

orientations $\boldsymbol{a}_0$ and $\boldsymbol{b}_0$, pseudo-invariants can be set up [44,45]. Aimène et al. [29] show that it is beneficial to use physically interpretable invariants. For this purpose

$$I_4 = \boldsymbol{a}_0 \cdot \boldsymbol{C} \cdot \boldsymbol{a}_0 = \lambda_{\mathrm{a}}^2, \tag{5}$$

$$I_6 = \boldsymbol{a}_0 \cdot \boldsymbol{C} \cdot \boldsymbol{b}_0, \tag{6}$$

$$I_8 = \boldsymbol{b}_0 \cdot \boldsymbol{C} \cdot \boldsymbol{b}_0 = \lambda_{\mathrm{b}}^2 \tag{7}$$

$$\text{and } I_{10} = \arccos(\boldsymbol{a}_0 \cdot \boldsymbol{b}_0) - \arccos\left(\frac{I_6}{\sqrt{I_4 I_8}}\right) = \gamma \tag{8}$$

are introduced, where I_4 and I_8 are the quadratic stretches λ_i^2 along a roving direction (i = a,b). Engineering strains are related via

$$\varepsilon_{ii} = \lambda_i - 1 = \sqrt{I_j} - 1 \tag{9}$$

for $j = 4$ for i = a and $j = 8$ for i = b. Invariant I_{10} represents the shear angle γ, i.e. the change in angle between the roving directions [36]. Subsequently, based on the assumption that these three invariants contribute to the total strain energy density, it can be formulated as

$$W_{\mathrm{tot}}(\boldsymbol{C}) = W_{\mathrm{tot}}(I_j) \tag{10}$$

with j = 4,8,10. Its derivation with respect to the RCG tensor results in

$$\boldsymbol{S} = 2\left(\frac{\partial W_{\mathrm{tot}}}{\partial I_4}\frac{\partial I_4}{\partial \boldsymbol{C}} + \frac{\partial W_{\mathrm{tot}}}{\partial I_8}\frac{\partial I_8}{\partial \boldsymbol{C}} + \frac{\partial W_{\mathrm{tot}}}{\partial I_{10}}\frac{\partial I_{10}}{\partial \boldsymbol{C}}\right). \tag{11}$$

which, together with the partial derivations of the invariants [29], yields the expression

$$\boldsymbol{S} = 2\left(\frac{\partial W_{\mathrm{tot}}}{\partial I_4}\boldsymbol{a}_0 \otimes \boldsymbol{a}_0 + \frac{\partial W_{\mathrm{tot}}}{\partial I_8}\boldsymbol{b}_0 \otimes \boldsymbol{b}_0\right) + \frac{\partial W_{\mathrm{tot}}}{\partial I_{10}} \cdot \frac{1}{\sqrt{I_4 I_8 - I_6^2}} \cdot \left[\boldsymbol{a}_0 \otimes \boldsymbol{b}_0 + \boldsymbol{b}_0 \otimes \boldsymbol{a}_0 - I_6\left(\frac{\boldsymbol{a}_0 \otimes \boldsymbol{a}_0}{I_4} + \frac{\boldsymbol{b}_0 \otimes \boldsymbol{b}_0}{I_8}\right)\right]. \tag{12}$$

2.2. Hyperelastic material model

2.2.1. General assumptions

Due to the differences between membrane and bending stiffnesses of woven fabrics, they are often characterized and modeled in a decoupled way [12,15–22,46]. For membrane behavior, a M3D3 or M3D4 element is coupled with a S3R or S4R element, respectively, with bending idealization in section integration, as depicted in Fig. 1. The present work focuses on the membrane behavior and the hyperelastic material model associated to the membrane element. It is assumed that, due to the fabric's two-dimensional structure, a plane stress state exists. Rate-, temperature- or degradation-induced changes in the mechanical properties are not considered in this work. However, care is taken to ensure that the model can be extended at any time to include these effects.

Based on the above assumptions together with recommendations stated by Werner et al. [14], a modular macroscopic material model in the framework of hyperelasticity is developed. Here, no energy dissipation is assumed and thus, all strain energy is stored in the deformation. This assumption is reasonable for non-cyclic deformations [36]. The associated constitutive equations are formulated in a parameterized way, so that they can easily be adapted for different fabrics. The corresponding parameters can be determined by means of experimental studies.

It is assumed that the total strain density energy W_{tot} can be decomposed into a tension–compression-dependent component W_{TC} and a shear-dependent component W_{S}. These terms need to be functions of the used invariants I_4, I_8 and I_{10} and are defined in the following sections.

2.2.2. Tension–compression behavior

The first assumption made for the tension–compression-dependent strain energy density W_{TC} is that it can be further subdivided into two components $W_{\mathrm{TC,a}}$ and $W_{\mathrm{TC,b}}$, representing the strain energy stored in deformation along fiber directions a and b, respectively. It is further assumed that the strain energy density for positive strains is different from that for negative strains. Consequently, a case differentiation is necessary:

$$W_{\mathrm{TC}}(I_4, I_8) = \begin{cases} W_{\mathrm{T,a}} + W_{\mathrm{T,b}} & \text{for } I_4 > 1 \text{ and } I_8 > 1 \\ W_{\mathrm{T,a}} + W_{\mathrm{C,b}} & \text{for } I_4 > 1 \text{ and } I_8 \leq 1 \\ W_{\mathrm{C,a}} + W_{\mathrm{T,b}} & \text{for } I_4 \leq 1 \text{ and } I_8 > 1 \\ W_{\mathrm{C,a}} + W_{\mathrm{C,b}} & \text{for } I_4 \leq 1 \text{ and } I_8 \leq 1. \end{cases} \tag{13}$$

It is essential to incorporate the uniaxial tensile behavior of the fabric correctly. As shown in Fig. 3(a), the typical stress–strain curve for this load case can be divided into two zones. In the first one, undulations along the tensile direction are reduced, while undulations in the transverse rovings are increased. This phenomenon is referred to as crimp interchange. In the second zone, the fibers under tension experience longitudinal stretch.

To fit this curve, a quadratic function

$$\widehat{\sigma}_{\mathrm{T},i} = \alpha_i \varepsilon_{ii}^2 + \beta_i \varepsilon_{ii} \tag{14}$$

with parameters α_i and β_i is used for uniaxial tension. After integration over the longitudinal strain ε_{ii} and with Eq. (9), the corresponding uniaxial strain energy densities in dependence on the invariants are

$$\widehat{W}_{\mathrm{T,a}} = a_{\mathrm{a}}(\sqrt{I_4} - 1)^3 + b_{\mathrm{a}}(\sqrt{I_4} - 1)^2 \tag{15}$$

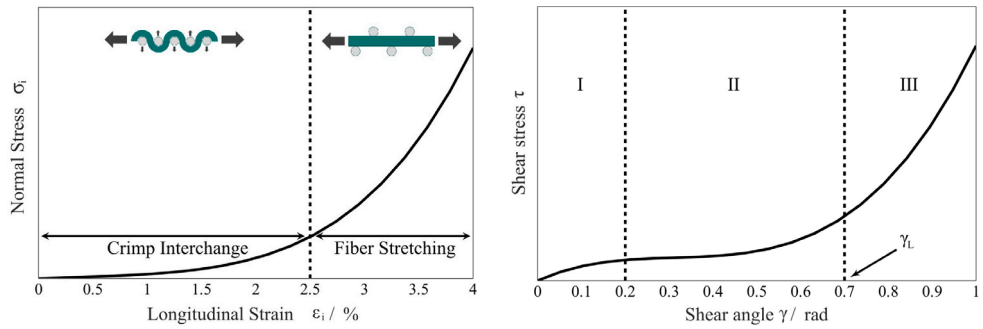

(a) Uniaxial tensile behavior according to [10]. (b) Shear behavior according to [7].

Fig. 3. Characteristic stress–strain curves of fabric structures.

and $$\widehat{W}_{\mathrm{T,b}} = a_{\mathrm{b}}(\sqrt{I_8}-1)^3 + b_{\mathrm{b}}(\sqrt{I_8}-1)^2. \tag{16}$$

The parameters a_i and b_i can be determined by means of uniaxial tensile test data.

Due to fiber–fiber-interactions, strain along one fiber direction induces not only longitudinal but also transverse stresses. Positive transverse strains hinder crimp interchange [5,10] and negative ones are assumed to facilitate fiber stretching and thus longitudinal tensioning. The following factors are introduced to model this behavior:

$$k_{\mathrm{TC,a}} = (1-p_{\mathrm{min,a}})\exp\left(c_a(\sqrt{I_8}-1)\right) + p_{\mathrm{min,a}} \tag{17}$$

and $$k_{\mathrm{TC,b}} = (1-p_{\mathrm{min,b}})\exp\left(c_b(\sqrt{I_4}-1)\right) + p_{\mathrm{min,b}}. \tag{18}$$

The tension–compression-parameter $p_{\mathrm{min,i}}$ is only allowed to attain values between 0 and 1, representing a complete reduction of the strain energy density for longitudinal tension at negative transverse strains and no reduction, respectively. While the tension–compression-parameter $p_{\mathrm{min,i}}$ limits the decrease for negative strains, the biaxial coupling coefficient c_{i} characterizes the interaction between the two roving directions. The exponential expression takes on positive values smaller or greater than 1 for negative or positive strains, respectively. Thus, the factors $k_{\mathrm{TC,a}}$ and $k_{\mathrm{TC,b}}$ are always positive. For negative transverse strains, they take on values between 0 and 1, causing a reduction of the strain energy density. For positive transverse strains, they are greater than 1 and lead to an increase of the strain energy density. Both parameters can be determined by experimental data of biaxial or uniaxial tests with lateral contraction. The corresponding strain energy densities are

$$W_{\mathrm{T,a}} = \widehat{W}_{\mathrm{T,a}} \cdot k_{\mathrm{TC,a}} \tag{19}$$

and $$W_{\mathrm{T,b}} = \widehat{W}_{\mathrm{T,b}} \cdot k_{\mathrm{TC,b}}. \tag{20}$$

At the moment, there are no published studies on the material behavior under in-plane compressive loading. As wrinkling of the textile may be partly hindered, e.g. by the adjacent mold or by metal layers in FML forming, combined stress states occur, and it can be assumed that the fabric's in-plane compressive behavior has to be taken into consideration. Transverse strains are assumed to have no influence on the longitudinal compression behavior, as no crimp interchange is expected under compression. A linear correlation between stresses and strains

$$\widehat{\sigma}_{\mathrm{C,i}} = \delta_{\mathrm{i}}\varepsilon_{\mathrm{i}} \tag{21}$$

is assumed. Hence, the corresponding strain energy densities along both roving directions in dependence on the invariants from Eq. (9) are

$$W_{\mathrm{C,a}} = d_{\mathrm{a}}(\sqrt{I_4}-1)^2 \tag{22}$$

and $$W_{\mathrm{C,b}} = d_{\mathrm{b}}(\sqrt{I_8}-1)^2. \tag{23}$$

The parameters d_{i} are proportional to the compressive stiffness and their values can be obtained from in-plane compression tests. These tests have not yet been performed, because a new test setup needs to be developed to avoid buckling of the fabric without inducing too much friction. A possible test setup can be found in [47]. An indirect method to determine the in-plane compressive stiffness could be the method presented by Dangora et al. [12]. Here, the in-plane compressive stiffness is calculated from the bending and tensile stiffnesses obtained by experimental results. Naujokaityte et al. [48] examined stability experiments on fabrics to calculated bending stiffnesses and the test method could be used in future work to identify the compression stiffness of fabrics. Selezneva et al. [49] assumed an in-plane compression stiffness of 10% of the tensile stiffness for heated self-reinforced polypropylene. Werner et al. [24] performed a numerical parameter study for FML forming and found compression stiffnesses of 0.1% to 1% of the tensile stiffness suitable for the not infiltrated fabric. The assumed material parameters can be found in Table 1.

2.2.3. Combined normal-shear behavior

Shear allows large deformations at comparatively small fiber strains and is therefore the dominant deformation mechanism in woven fabrics [9]. For the formulation of the shear-dependent strain energy density, the correct description of the pure shear deformation is essential. Fig. 3(b) depicts the characteristic stress curve for pure shear as a function of the shear angle γ. In the first zone (I), pure rigid body rotations of the rovings take place and the low shear stresses can be attributed to the friction in the contact points at crossovers. As soon as the rovings come into lateral contact with each other, they start compacting accompanied by an increase in tension, which is visible in zone II. The transition between zones II and III is marked by the critical shear angle γ_{L}, which is often referred to as locking angle. In the locking zone (III) further shear deformation induces large shear stresses [7,25]. A third-degree polynomial of type

$$\tau_{\mathrm{S}} = s_1\gamma + s_2\gamma^2 + s_3\gamma^3 \tag{24}$$

is chosen to describe this behavior, leading to the corresponding strain energy density

$$W_{\mathrm{S}} = \frac{1}{2}s_1 I_{10}^2 + \frac{1}{3}s_2 I_{10}^3 + \frac{1}{4}s_3 I_{10}^4. \tag{25}$$

The shear angle has been replaced by the invariant I_{10} from Eq. (8) and the parameters can be determined using picture frame or bias-extension tests.

Experimental studies showed that membrane tensions also influence the shear behavior of fabrics. Positive fiber strains lead to increased shear stresses for a given shear deformation [7,9]. Negative fiber strains are assumed to lower the necessary energy to reach a given shear deformation as the contact forces at the crossovers are reduced. Thus, two coupling terms are introduced for each roving direction, describing the shear behavior under membrane tension or compression along that direction. Depending on the present load case, the strain energy density is adjusted accordingly. If no membrane strains are present, the

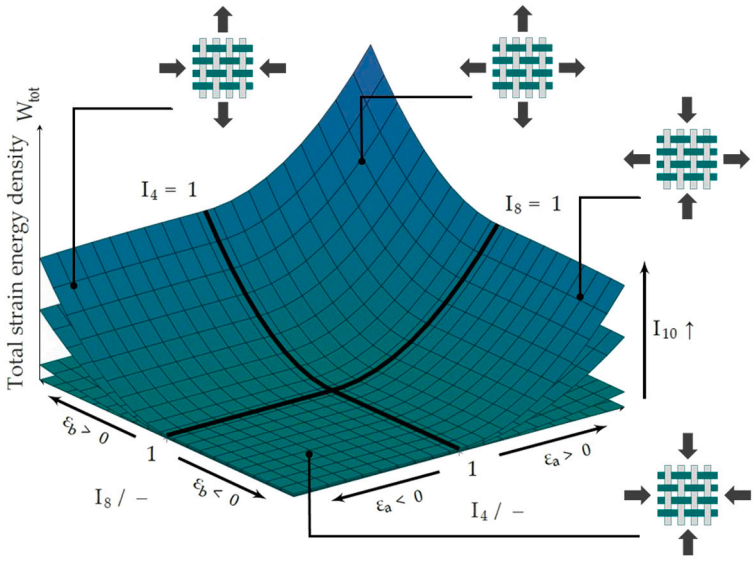

Fig. 4. Qualitative strain energy density in dependence on the invariants I_4, I_8 and I_{10}.

terms do not influence the pure shear behavior. The parameters can be determined by means of pre-stretched picture frame or bias-extension tests.

For positive strains, the corresponding additional strain energy density is expressed via

$$W_{\mathrm{ST,a}} = \frac{1}{3} I_{10}^3 \, s_{\mathrm{T,a}} (I_4 - 1)^2 \tag{26}$$

$$W_{\mathrm{ST,b}} = \frac{1}{3} I_{10}^3 \, s_{\mathrm{T,b}} (I_8 - 1)^2. \tag{27}$$

with the tension–shear-parameter $s_{\mathrm{T,i}}$. In the presence of negative strains, the shear strain energy density is reduced by multiplication with the exponential factors

$$k_{\mathrm{SC,a}} = \exp(s_{\mathrm{C,a}} (I_4 - 1)^3) \tag{28}$$

$$k_{\mathrm{SC,b}} = \exp(s_{\mathrm{C,b}} (I_8 - 1)^3) \tag{29}$$

which contain the compression-shear-parameter $s_{\mathrm{C,i}}$. A simple subtractive reduction could lead to negative strain energy densities. To ensure a smooth asymptotic reduction of the strain energy density without reaching a value of zero or below, a multiplication is chosen. The exponential term guarantees that the expression only takes on values greater than zero and less or equal to one for negative normal strains.

2.2.4. Total material behavior

The total strain energy density is composed additively by the equations described in the preceding sections:

$$W_{tot} = \begin{cases} W_{\mathrm{T,a}} + W_{\mathrm{T,b}} + W_{\mathrm{S}} + W_{\mathrm{ST,a}} + W_{\mathrm{ST,b}} & \text{for } I_4 > 1 \text{ and } I_8 > 1 \\ W_{\mathrm{T,a}} + W_{\mathrm{C,b}} + \left(W_{\mathrm{S}} + W_{\mathrm{ST,a}}\right) \cdot k_{\mathrm{SC,b}} & \text{for } I_4 > 1 \text{ and } I_8 \leq 1 \\ W_{\mathrm{C,a}} + W_{\mathrm{T,b}} + \left(W_{\mathrm{S}} + W_{\mathrm{ST,b}}\right) \cdot k_{\mathrm{SC,a}} & \text{for } I_4 \leq 1 \text{ and } I_8 > 1 \\ W_{\mathrm{C,a}} + W_{\mathrm{C,b}} + W_{\mathrm{S}} \cdot k_{\mathrm{SC,a}} \cdot k_{\mathrm{SC,b}} & \text{for } I_4 \leq 1 \text{ and } I_8 \leq 1. \end{cases} \tag{30}$$

The corresponding energy surfaces are depicted qualitatively as a function of the invariants I_4 and I_8 in Fig. 4 for selected shear angles I_{10}. The bold lines $I_4 = 1$ and $I_8 = 1$ represent uniaxial load along roving orientations $\boldsymbol{a}$ and $\boldsymbol{b}$, respectively.

2.2.5. Implementation

The hyperelastic approach including the material equations derived in the previous sections was implemented into an Abaqus/Explicit user subroutine VUMAT. The flowchart in Fig. 5 visualizes the setup. The

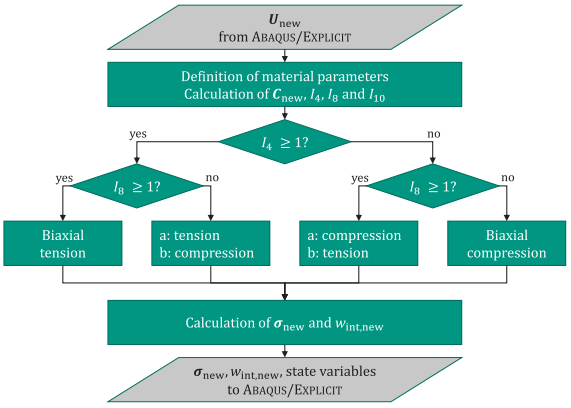

Fig. 5. Flowchart of the VUMAT-subroutine for Abaqus/Explicit.

right stretch tensor U of the actual step is imported from Abaqus/Explicit. The RCG tensor C in Eq. (3) and the invariants are calculated according to Eqs. (5) to (8). At the end of the subroutine, the Cauchy-stress tensor $\boldsymbol{\sigma}$ in Eq. (4), the weight specific internal energy w_{int} and the state variables for visualization, like the invariants, are calculated and passed to Abaqus/Explicit.

The experiments to identify all parameters of the material model are summarized in Fig. 6. A Matlab-script is used to determine the parameters from experimental data, using nonlinear regression. In a first step, the equations of uniaxial tension–compression and pure shear behavior are fit to the experimental data and in a second step, the parameters describing the coupling mechanisms are identified. In the event that not all values can be determined experimentally, additional assumptions can be made or mechanisms can be deactivated owing to the modular setup of the equations. For balanced fabrics, the maximum number of 17 independent parameters reduces to 10 as both roving directions have identical material properties.

3. Results and discussion

3.1. Material data

To verify the presented material model and to demonstrate its functionality, data from literature are used. The work of Komeili [50]

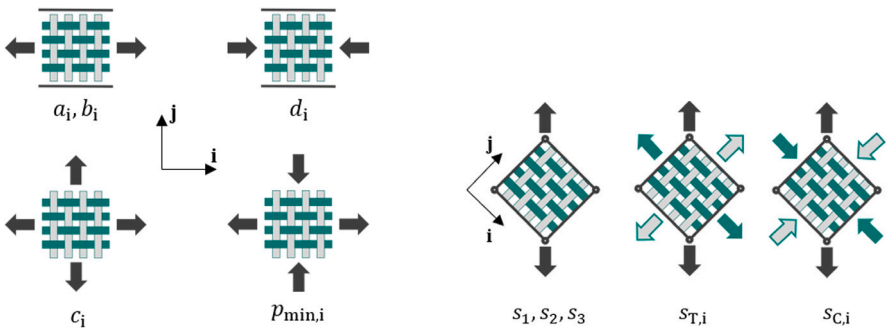

(a) Tension-compression behavior (b) Shear behavior

Fig. 6. Experimental investigations to determine the material parameters.

Table 1
Parameter values used for validation and numerical calculations.

Material behavior	Parameter	Value	Determined
Uniaxial tension	$a_a = a_b$	4130.00 MPa	1st regression
	$b_a = b_b$	667.50 MPa	1st regression
Uniaxial compression	$d_a = d_b$	0.65 MPa	Assumption
Biaxial	$p_{min,a} = p_{min,b}$	0.75	Assumption
Tension–compression	$c_a = c_b$	23.67	2nd regression
Pure shear	s_1	25.06×10^{-3} MPa	1st regression
	s_2	-186.79×10^{-3} MPa	1st regression
	s_3	562.39×10^{-3} MPa	1st regression
Tension–shear	$s_{T,a} = s_{T,b}$	1467.60 MPa	2nd regression
Compression-shear	$s_{C,a} = s_{C,b}$	100.00	Assumption

permits direct determination of 7 out of 10 parameters for a balanced plain-weave fabric. These parameters describe the uni- and biaxial tension and shear behavior and are determined with the aid of the aforementioned MATLAB-script. For parameters associated with the material's in-plane compression behavior (d_i, $p_{min,i}$, $k_{SC,i}$), assumptions are made which are evaluated and discussed with the aid of numerical simulations in Section 3.4.1. Table 1 lists the set of material parameters used in the following calculations. The material is modeled with a thickness of 1 mm and a density of 0.75 g cm^{-3}.

3.2. Analytical-numerical validation

The material model was validated using a single M3D4 element. The results of numerical calculations for uniaxial, biaxial and shear load cases were compared with those of analytical calculations to ensure the correct implementation of the constitutive equations. In a subsequent step, the ABAQUS/EXPLICIT built-in FABRIC-model was fit to the same material data and identical calculations were performed. The results of both material models are compared in Fig. 7 and show good agreement for longitudinal tension or compression (Figs. 7(a) and 7(c)) and shear stresses (Fig. 7(d)). Moreover, it can be found that the newly developed material model induces stresses transverse to the tensile direction for constrained uniaxial loading in Fig. 7(a) and shows higher longitudinal stresses under biaxial loading compared to the ABAQUS/EXPLICIT built-in FABRIC-model in Fig. 7(b). To further investigate the consequences on the overall deformation behavior, a tensile and bias-extension test specimen with multiple elements is considered in Section 3.3.

3.3. Tensile and bias-extension tests to check for physically meaningful material behavior

In the following, a fabric sample of dimensions 200 mm × 50 mm ($L \times B$) is created with 10,000 M3D3 elements and a strain of 3% is applied along $\boldsymbol{x}$ for the uniaxial tensile test in Fig. 8. For the bias-extension test in Fig. 9, a strain of 10% is applied along $\boldsymbol{x}$. Rigid clampings at the short edges hinder relative movement of the rovings. In this qualitative analysis, no bending elements are considered, because the membrane behavior of the two material models, ABAQUS/EXPLICIT built-in FABRIC-model and hyperelastic model, are compared. In reality, excessive loading could lead to shear locking of the fabric and thus to bending deformation in the fabric. For comparison with experimental data and validation of the material model, the bending behavior has to be considered in a decoupled manner, as shown in Fig. 1 and applied for forming simulation in Section 3.4.

Fig. 8 depicts the resulting strains along roving directions 1 and 2 for both material models under uniaxial tension. With the FABRIC-model, no displacements occur in the y-direction, whereas the hyperelastic material model predicts a transverse contraction of about −15% in ε_{22} direction in Fig. 8(c). The transverse strains induce shear deformations in the hyperelastic model in the clamping regions, as shown in Fig. 8(d). The magnitudes of the ε_{11}-components are in the same range for both material models.

Fig. 9 depicts the resulting strains along roving directions 1 and 2 for both material models in the bias-extension test. Due to the pure shear loading in the bias-extension test, both material models behave identically, and no tensile strains are induced using the hyperelastic model, which is in good agreement with the single-element test results in Fig. 7(d) and can be explained by Eq. (25). Inducing tensile strains subsequent to pure shear loading would correspond to shear–tension coupling, which is not captured by the model, because either shear–tension or tension–shear coupling can be modeled due to interdependence.

To identify the part of the hyperelastic material model responsible for the transverse strain effect under tensile loading, the results of analog calculations with modified versions of the subroutine were examined under tensile loading. With completely deactivated coupling mechanisms (Fig. 10(a)), the predicted material behavior corresponds very closely to that of the FABRIC-model. Lateral contractions and transverse strains are only observed with the biaxial coupling (Fig. 10(b)), which causes strains ε_{11} in the 1-direction to induce transverse strains ε_{22}. While these strains arise along the 2-direction in the central part of the specimen, strains close to the clampings are not possible due to the local boundary conditions. The resulting shape of the fabric can also be observed in experimental studies on tensile test specimens, as shown in Fig. 10(d) qualitatively [51]. Thus, the biaxial coupling is essential for the numerical calculation of fabric structures undergoing normal strains.

3.4. Parameter analysis in double-dome forming

To verify the functionality of the hyperelastic material model in more complex simulations, the deformation behavior of a flat, not yet infiltrated FML was calculated. The FML consisted of three fabric

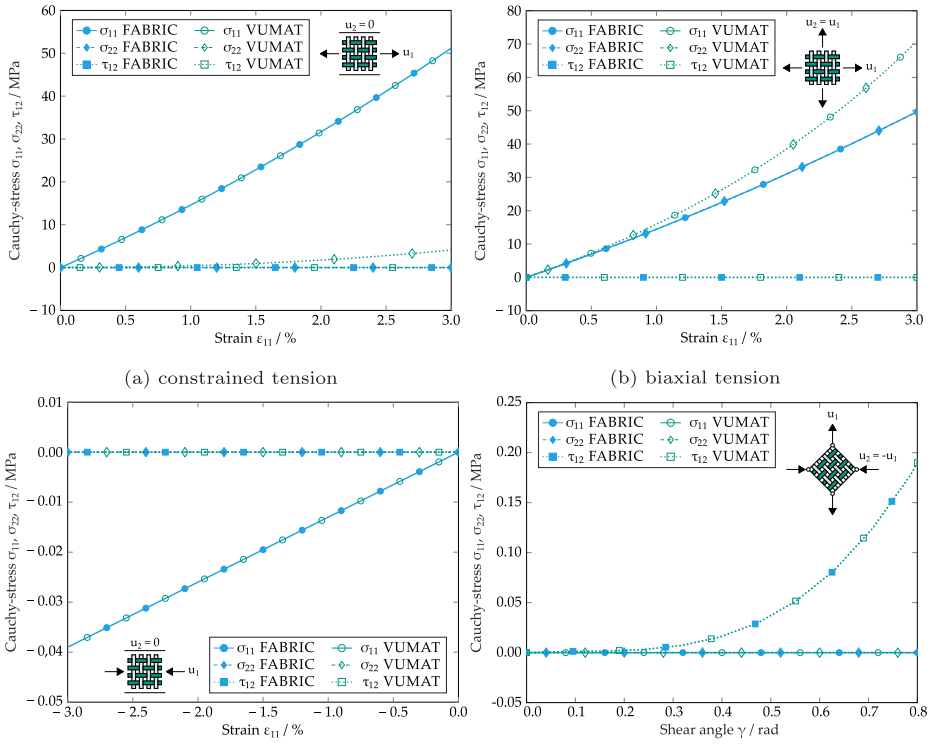

(a) constrained tension

(b) biaxial tension

(c) constrained in-plane compression

(d) picture frame test with pure shear

Fig. 7. Numerical verification and comparison of Abaqus/Explicit built-in Fabric-model and hyperelastic material based on single element M3D4 models.

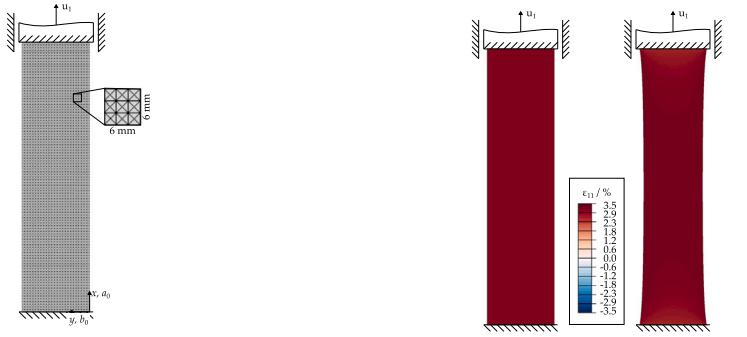

(a) Mesh and orientation of material
x, y global coordinate system
a, b material coordinate system

(b) ε_{11} / % Fabric-model (left), hyperelastic model (right)

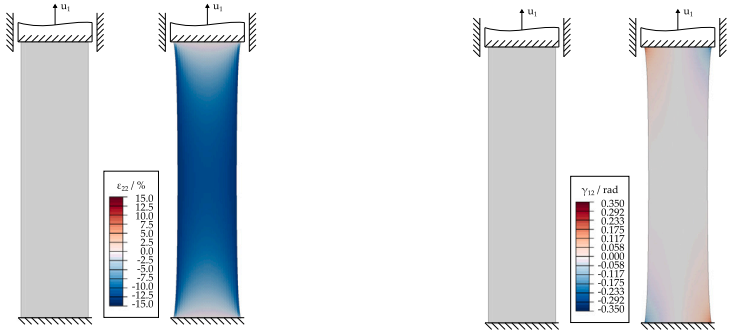

(c) ε_{22} / %: Fabric-model (left), hyperelastic model (right)

(d) γ_{12} / rad: Fabric-model (left), hyperelastic model (right)

Fig. 8. Comparison of strains for uniaxial tensile test.

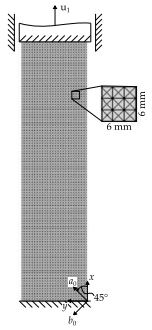

(a) Mesh and orientation of material
x, y global coordinate system
a, b material coordinate system

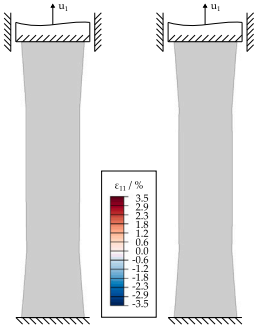

(b) ε_{11} / %
FABRIC-model (left),
hyperelastic model (right)

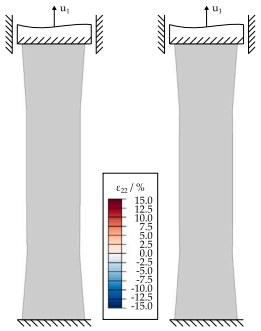

(c) ε_{22} / %:
FABRIC-model (left),
hyperelastic model (right)

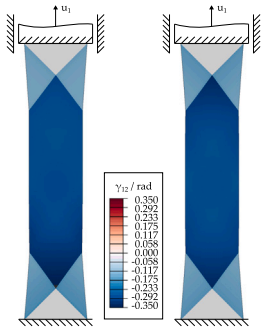

(d) γ_{12} / rad:
FABRIC-model (left),
hyperelastic model (right)

Fig. 9. Comparison of strains for bias-extension test.

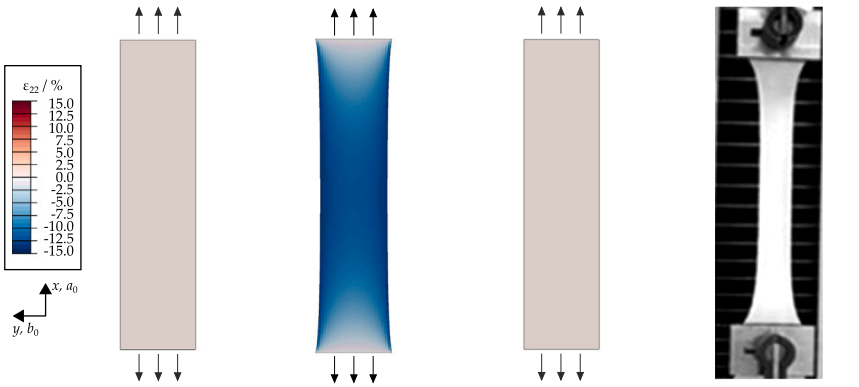

(a) no coupling (b) only biaxial coupling (c) only normal-shear coupling (d) Experimental tensile test [51]

Fig. 10. ε_{22}-component for different modified subroutines for uniaxial tensile test.

plies, initially oriented along the global $x - y$-coordinates, and two metallic cover layers. Each fabric ply was modeled with 20,268 M3D3 elements for membrane behavior, stacked with 20,268 corresponding S3R elements with bending idealization in section integration, to account for bending behavior of the fabric, as depicted in Fig. 11. The fabric material properties are summarized in Table 1 for membrane behavior of the fabric and in Table 2 for bending behavior of the fabric. The fabric membrane data are based on literature data from Komeili et al. [50]. Komeili does not provide any data on the bending behavior of the material, as bending was not modeled. A previous parameter study for dry FML forming, performed by Werner et al. [24], showed little influence of the fabric bending stiffness on the forming result, due to the encasing metal layers and high blank holder pressures of 2 MPa. The fabric bending stiffness is therefore assumed with 100 MPa in both roving directions. In the parametric study, the compressive stiffness has also been evaluated and is therefore assumed to be 1.3 MPa. Every single metal layer consists of 13,568 S3R elements and the metal behavior is modeled elastic–plastic with isotropic hardening, but without damage initiation or failure, according to tensile tests performed and described by Werner et al. [23,24]. The tools are assumed to be ideally stiff compared to the metal and fabric plies and are therefore modeled as rigid discrete bodies. The contact between the tools and plies is

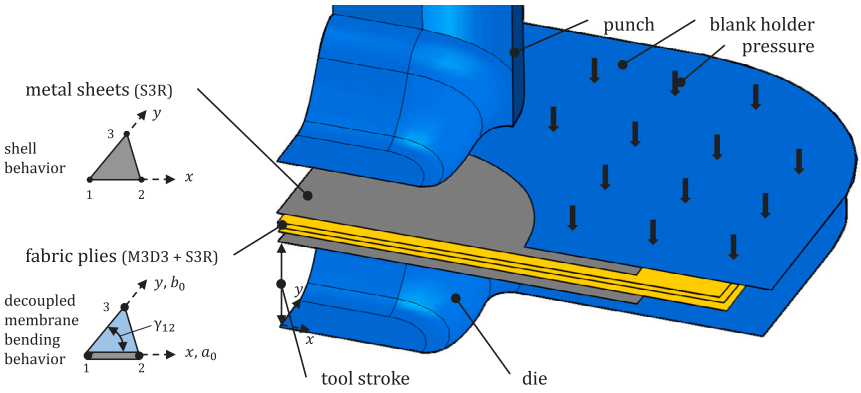

Fig. 11. Double dome geometry: quarter FE-model of tool and FML [24] modified geometry from [41].

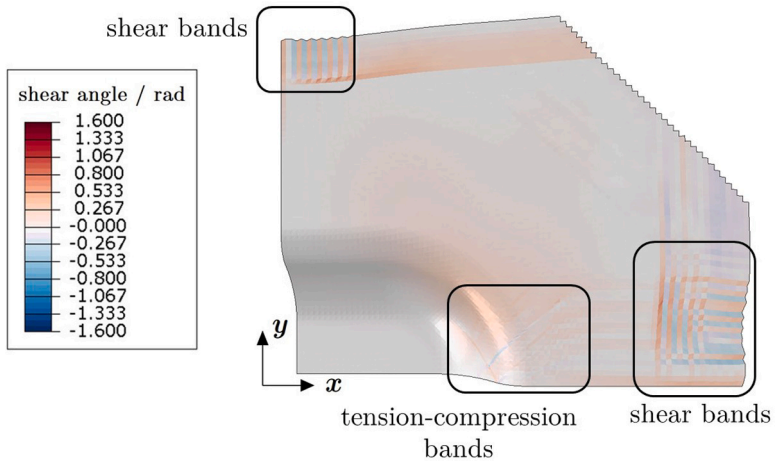

Fig. 12. Shear angle distribution for disabled tension–compression coupling at $p_{\min,i} = 0$.

Table 2
Material and contact parameters for double-dome forming model. b := bending, tm := tool–metal; mf := metal–fabric, ff := fabric–fabric.

Model parameter	Constant	Value
Steel DC04	$E, \nu, R_{p0.05}$	186.6 GPa, 0.3, 159.0 MPa
Fabric bending	$E_{b,11} = E_{b,22}, \nu_{12}$ $G_{12} = G_{13} = G_{23}$	100.0 MPa, 0.0 1.0 MPa
Normal contact Tangential contact	c_n $\mu_{tm}, \mu_{mf}, \mu_{ff}$	1000.0 MPa 0.1, 0.25, 0.334

modeled with the Abaqus/Explicit built-in general contact and specified tangential contact pairings for tool–metal (μ_{tm}), metal–fabric (μ_{mf}) and fabric–fabric (μ_{ff}) contact with the parameters in Table 2. For the normal contact, a penalty contact stiffness of $c_n = 1000$ MPa is used to speed up the simulation. Lower values would increase the simulation speed, but would lead to intersection of the tools and plies. For the membrane behavior, the hyperelastic material model and the Fabric-model are used in the scope of this work. In the following sections, the middle fabric layer is visualized.

3.4.1. Analysis of compression-related material parameters

The parameters $p_{\min,i}$, d_i and $s_{C,i}$ have been set by assumptions. To investigate their influence on the draping, calculations are performed for different parameter values. The tension–compression-parameter $p_{\min,i}$ was varied in seven steps between zero and one. Values of $p_{\min,i}$ below 0.25 led to erroneous formation of tension–compression bands as shown in Fig. 12, which cannot be observed in experimental studies [24]. The effect was not influenced by d_i and $s_{C,i}$. To avoid it, a value of $p_{\min,i} = 0.75$ was used hereafter. Additionally, shear bands occurred in the areas of large fiber displacement outside the metallic cover layers, but a variation of $p_{\min,i}$ showed no influence on their formation. The parameter d_i was proportional to the compressive stiffness E_C, which was varied from 0.13 MPa to the material's initial tensile stiffness 1300 MPa in powers of ten. For low values of E_C, the shear bands vanished, accompanied by high compressive strains. As can be seen in Fig. 13, with increasing compressive stiffness the shear bands became more pronounced and expanded toward the center of the part while outside the metallic cover layers, formation of wrinkles is promoted. To avoid the occurrence of very large strains and strong shear bands, the values 0.13 MPa, 1.3 MPa and 13 MPa were further considered. The compression-shear-parameter $s_{C,i}$ was varied between 10 and 1000 in powers of ten. Fig. 14 shows the resulting shear angles for a compressive stiffness of $E_C = 1.3$ MPa. High values of $s_{C,i}$ facilitated the formation of shear bands due to the reduction of the necessary energy to induce shear deformation at negative membrane strains. Additional calculations were performed to further investigate the cause of shear bands. The outcome indicated that the formation of shear bands results from a low shear stiffness compared to the in-plane compressive stiffness and instabilities under in-plane compression [24]. High in-plane compressive stresses were relieved by changing from in-plane compression to shear deformation, which is more energy-efficient. As only in-plane stress states are considered, the shear behavior in this model was not influenced by three-dimensional

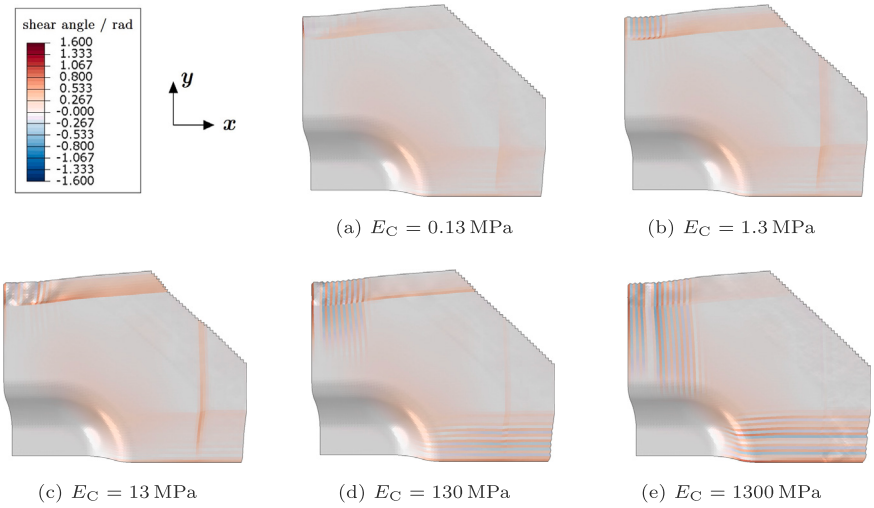

Fig. 13. Shear angle distribution for different values of the compressive stiffness E_C for double dome geometry.

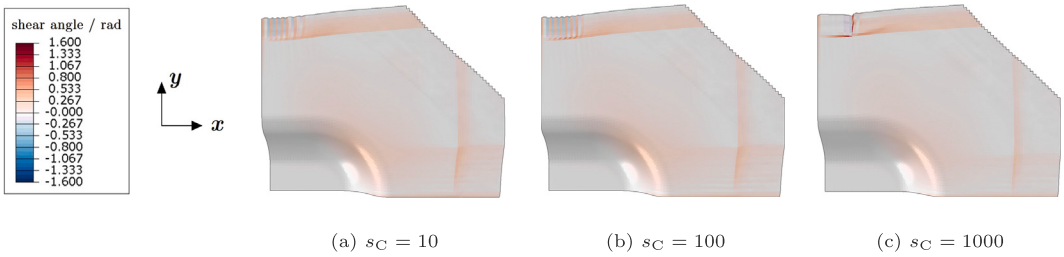

Fig. 14. Shear angle distribution for different values of the compression-shear parameter s_C for double dome geometry.

effects. In reality, higher in-plane shear stiffnesses can be expected due to an increase of internal friction, if out-of-plane-thickening is hindered and compressive stresses occur in this direction. Accordingly, an extension of the model toward three-dimensional stress states might avoid the occurrence of shear bands. In addition to the experimental determination of the model parameters, further investigations on the bending behavior are indispensable to model the material behavior fully. The bending behavior is of particular interest when it comes to formation of wrinkles.

3.4.2. Analysis of the coupling mechanisms

Again, different configurations of the newly developed material model were used and the results were compared to those obtained with the Fabric-model. The subroutine allows transient element-wise tracking of present strain states as visualized in Fig. 15. All four possible biaxial strain states occur in the deformed component. The contour of the metal sheets bounds the zones in which positive strains overlap with negative transverse strains. In the center of the component, the fabric is stretched biaxially. Comparisons of calculations with activated and deactivated coupling mechanisms show that the biaxial coupling leads to a slightly changed boundary between the areas of biaxial tensile strains and tensile-compressive strains in the region of the strongest curvature.

Fig. 16 shows the strains ϵ_{11}, ϵ_{22} and the shear angle γ_{12} for three paths in x-, 45° and y-direction. In addition, the inner punch radius, the outer punch radius and the metal sheet contour are shown. Each plotted value in Figs. 16(b) to 16(j) is the average of the eight surrounding elements of the depicted node. The Fabric-model, the Vumat-subroutine without couplings and the Vumat-subroutine with shear coupling show almost identical results along the paths.

Only for the γ_{12}-path in Fig. 16(d), the three models show different values, which can be attributed to formation of shear bands due to the metal sheet. The shear bands can be considered as numerical instabilities and are therefore not equal in any of the calculated models. The shear coupling favors the shear band formation, because the model with shear coupling, as well as the model with complete couplings, show largely the same curves, as well as the highest shear angles. The models with biaxial coupling and complete coupling show very similar strain and shear angle curves for all three paths. Compared to the models without biaxial coupling, the models with biaxial coupling show lower strains in the punch region and predict higher absolute strains in the ϵ_{11} and ϵ_{22} directions between the two radii (higher stretching in Figs. 16(b), 16(i) and compression in the transverse direction in Figs. 16(c), 16(h), respectively). The maximum shear angle in 45°-direction in Fig. 16(g) is only slightly affected by the biaxial coupling, while the shear coupling has no influence on the maximum shear angle. The slight influence is attributed to a small shear angle, which is about 20°. The shear angle jump in Fig. 16(j) results from shear band formation on the metal sheet contour for all models.

3.5. Discussion of the material model

The results of the preceding calculations reveal that the coupling of strain components contributes significantly to the deformation behavior of fabric structures and should be considered for draping processes with constrained out-of-plane deformations, like high blank holder pressures. For forming conditions with low longitudinal strains or low compression forces in thickness direction, the biaxial coupling may be neglected, as the forming process can be considered as free draping process with pure shear deformations. In free draping processes, the not investigated shear–tension coupling seems to be more relevant.

As all possible strain states of combined tension and compression occur in the results, it can be deduced that negative membrane strains should not be neglected. Due to a lack of experimental data, the in-plane compression parameters are currently estimated based on assumptions and need to be determined with the aid of suitable

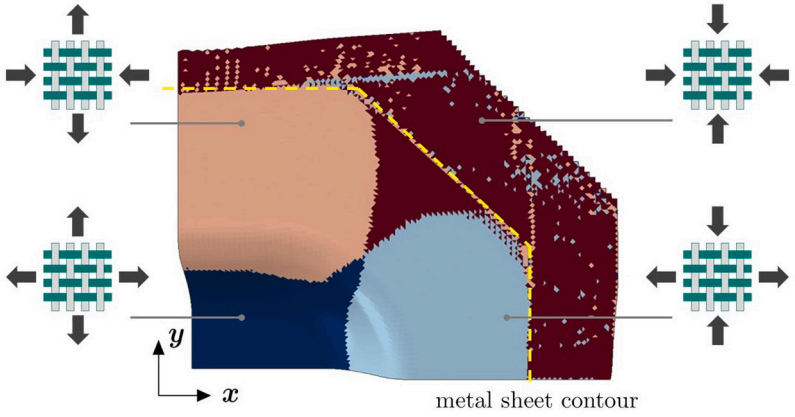

Fig. 15. Distribution of the four possible biaxial strain states.

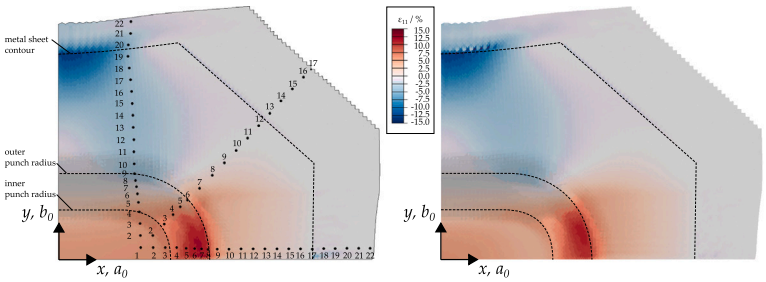

(a) Path along x-, 45°-, y-direction and ε_{11} strains for FABRIC-model (left) and hyperelastic model (right)

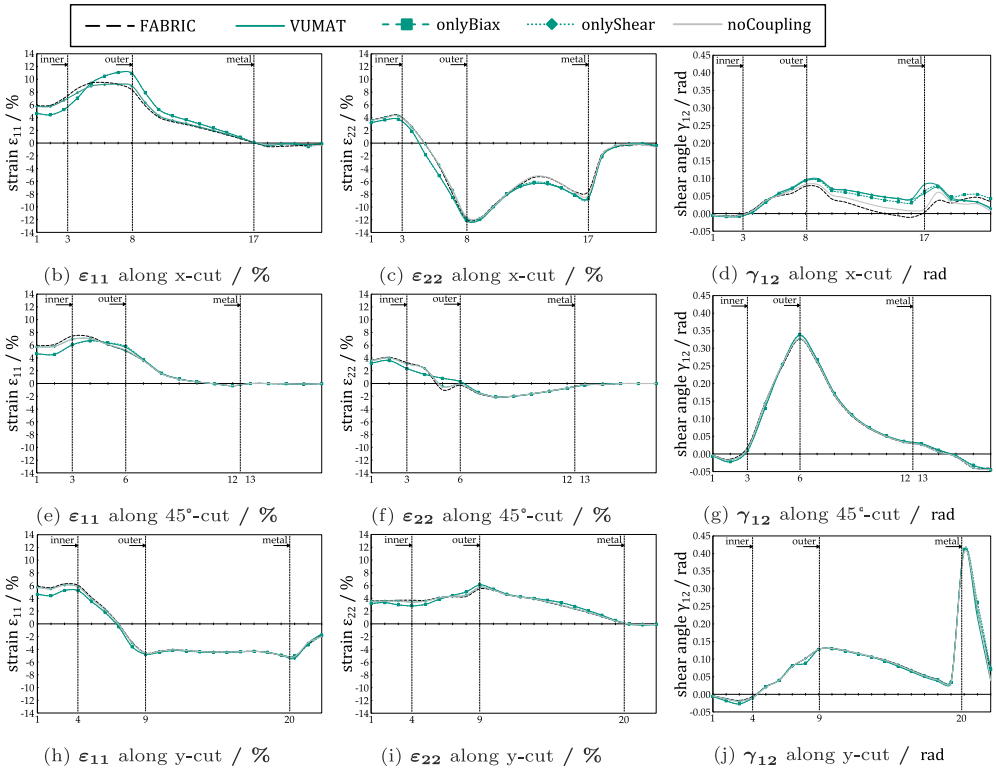

(b) ε_{11} along x-cut / % (c) ε_{22} along x-cut / % (d) γ_{12} along x-cut / rad

(e) ε_{11} along 45°-cut / % (f) ε_{22} along 45°-cut / % (g) γ_{12} along 45°-cut / rad

(h) ε_{11} along y-cut / % (i) ε_{22} along y-cut / % (j) γ_{12} along y-cut / rad

Fig. 16. Strains ϵ_{11}, ϵ_{22} and γ_{12} along x-, 45°- and y-path for FABRIC-model and hyperelastic model with different activated couplings.

experimental investigations in future. As it can be deduced from the double-dome forming calculations, shear behavior should be modeled as fiber-strain dependent only for large shear angles. For calculations with high normal strains, the influence of the biaxial coupling may exceed the one of the normal-shear coupling, but both contribute noticeably to the final result. Especially, the coupling of positive and negative normal strains enables realistic fabric material behavior, as shown in Fig. 10 for the tensile test.

Compared to conventional material models based on Cauchy-elasticity, this hyperelastic approach allows formulation of the constitutive equations with respect to the material's initial configuration. An extension to three-dimensional stress states is possible and desirable, as experimental investigations indicate the relevance of out-of-plane-stresses in case of high deformation forces [52,53]. The hyperelastic, invariant-based models developed by Boisse et al. [28,54–59] use the same set of invariants and their approach for three-dimensional stress states could be used. Experimental studies revealed that liquid matrix has an influence on the deformation behavior of fabrics [60]. To model simultaneous forming and infiltration, the material model can be extended to include viscoelastic effects [20,60].

4. Conclusion

A hyperelastic, invariant-based material model was developed to describe the deformation behavior of woven fabric structures in forming simulations. The material model takes into account biaxial tension–compression behavior, as well as normal strain-dependent shear behavior for positive and negative strains. The modular architecture of the constitutive equations allows for easy adaptation of the model to different materials and for identification of the parameters by independent experimental investigations.

The material model is conditioned using data from literature and assumptions concerning the compressive behavior. It was demonstrated and further investigated in numerical calculations of a tensile test specimen and a double-dome geometry, showing promising outcomes. Comparisons with results obtained using the Abaqus/Explicit Fabric-model reveal that the hyperelastic material model yields more realistic results and that biaxial tension–compression coupling is of particular importance. It is particularly suitable for forming processes where high normal stresses are expected due to grippers, blank holders or encasing layers of high stiffness. When large shear angles are expected, consideration of the normal-shear coupling is recommended. It shows particular influence on the shear stresses for models with low normal stresses.

Due to the lack of experimental data in the negative strain region, the material model is subject to uncertainties. Consequently, the next step to enhance the model's applicability is to experimentally examine a complete set of material data, especially for combined strain states and under compressive loading. Future perspectives are to extend the material model toward three-dimensional stress states and the influence of liquid matrix.

CRediT authorship contribution statement

Florian Schäfer: Methodology, Software, Verification, Formal analysis, Investigation, Writing – original draft, Writing – review, Visualization. **Henrik O. Werner:** Software, Resources, Visualization, Writing – review & editing. **Frank Henning:** Funding acquisition. **Luise Kärger:** Supervision, Writing – review.

Declaration of competing interest

The authors declare that they have no known competing financial interests or personal relationships that could have appeared to influence the work reported in this paper.

Data availability

Data will be made available on request.

Acknowledgments

The German Research Foundation (DFG) kindly supports this research project (HE 6154/4-2, KA 4224/6-1). Moreover, the authors thank their colleagues for support, especially Nils Meyer, Christian T. Poppe and Constantin Krauß.

References

[1] Mayyas A, Qattawi A, Omar M, Shan D. Design for sustainability in automotive industry: A comprehensive review. Renew Sustain Energy Rev 2012;16(4):1845–62. http://dx.doi.org/10.1016/j.rser.2012.01.012.

[2] Görthofer J, Meyer N, Pallicity TD, Schöttl L, Trauth A, Schemmann M, Hohberg M, Pinter P, Elsner P, Henning F, Hrymak A, Seelig T, Weidenmann K, Kärger L, Böhlke T. Virtual process chain of sheet molding compound: Development, validation and perspectives. Composites B 2019;169:133–47. http://dx.doi.org/10.1016/j.compositesb.2019.04.001.

[3] Kärger L, Bernath A, Fritz F, Galkin S, Magagnato D, Oeckerath A, Schön A, Henning F. Development and validation of a CAE chain for unidirectional fibre reinforced composite components. Compos Struct 2015;132:350–8. http://dx.doi.org/10.1016/j.compstruct.2015.05.047, URL http://www.sciencedirect.com/science/article/pii/S0263822315004213.

[4] Kärger L, Galkin S, Zimmerling C, Dörr D, Linden J, Oeckerath A, Wolf K. Forming optimisation embedded in a CAE chain to assess and enhance the structural performance of composite components. Compos Struct 2018;192:143–52. http://dx.doi.org/10.1016/j.compstruct.2018.02.041.

[5] Boisse P, Buet K, Gasser A, Launay J. Meso/macro-mechanical behaviour of textile reinforcements for thin composites. Compos Sci Technol 2001;61(3):395–401. http://dx.doi.org/10.1016/s0266-3538(00)00096-8.

[6] Hivet G, Boisse P. Consistent mesoscopic mechanical behaviour model for woven composite reinforcements in biaxial tension. Composites B 2008;39(2):345–61. http://dx.doi.org/10.1016/j.compositesb.2007.01.011.

[7] Launay J, Hivet G, Duong AV, Boisse P. Experimental analysis of the influence of tensions on in plane shear behaviour of woven composite reinforcements. Compos Sci Technol 2008;68(2):506–15. http://dx.doi.org/10.1016/j.compscitech.2007.06.021.

[8] Dixit A, Mali HS. Modeling techniques for predicting the mechanical properties of woven-fabric textile composites: a review. Mech Compos Mater 2013;49(1):1–20. http://dx.doi.org/10.1007/s11029-013-9316-8.

[9] Nosrat-Nezami F, Gereke T, Eberdt C, Cherif C. Characterisation of the shear–tension coupling of carbon-fibre fabric under controlled membrane tensions for precise simulative predictions of industrial preforming processes. Composites A 2014;67(67):131–9. http://dx.doi.org/10.1016/j.compositesa.2014.08.030.

[10] Kashani MH, Hosseini A, Sassani F, Ko FK, Milani AS. Understanding different types of coupling in mechanical behavior of woven fabric reinforcements: A critical review and analysis. Compos Struct 2017;179:558–67. http://dx.doi.org/10.1016/j.compstruct.2017.06.069.

[11] Dangora LM, Hansen CJ, Mitchell CJ, Sherwood JA, Parker JC. Challenges associated with shear characterization of a cross-ply thermoplastic lamina using picture frame tests. Composites A 2015;78:181–90. http://dx.doi.org/10.1016/j.compositesa.2015.08.015.

[12] Dangora LM, Mitchell CJ, Sherwood JA. Predictive model for the detection of out-of-plane defects formed during textile-composite manufacture. Composites A 2015;78:102–12. http://dx.doi.org/10.1016/j.compositesa.2015.07.011.

[13] White KD, Sherwood JA. Finite element simulation of thickness changes in laminate during thermoforming. In: Proceedings of the international conference of global network for innovative technology and AWAM international conference in civil engineering. AIP conference proceedings 1896, 030033, 2017, http://dx.doi.org/10.1063/1.5008020.

[14] Werner HO, Schäfer F, Henning F, Kärger L. Material modelling of fabric deformation in forming simulation of fiber-metal laminates – A review on modelling fabric coupling mechanisms. In: ESAFORM 2021. 2021, http://dx.doi.org/10.25518/esaform21.2056.

[15] Boisse P, Akkerman R, Carlone P, Kärger L, Lomov SV, Sherwood JA. Advances in composite forming through 25 years of ESAFORM. Int J Mater Form 2022;15(39). http://dx.doi.org/10.1007/s12289-022-01682-8.

[16] Soulat D, Cheruet A, Boisse P. Simulation of continuous fibre reinforced thermoplastic forming using a shell finite element with transverse stress. Comput Struct 2006;84(13–14):888–903. http://dx.doi.org/10.1016/j.compstruc.2006.02.011.

[17] Boisse P, Hamila N, Vidal-Sallé E, Dumont F. Simulation of wrinkling during textile composite reinforcement forming. Influence of tensile, in-plane shear and bending stiffnesses. Compos Sci Technol 2011;71(5):683–92. http://dx.doi.org/10.1016/j.compscitech.2011.01.011.

[18] Allaoui S, Boisse P, Chatel S, Hamila N, Hivet G, Soulat D, Vidal-Salle E. Experimental and numerical analyses of textile reinforcement forming of a tetrahedral shape. Composites A 2011;42(6):612–22. http://dx.doi.org/10.1016/j.compositesa.2011.02.001.

[19] Haanappel SP, ten Thije R, Sachs U, Rietman B, Akkerman R. Formability analyses of uni-directional and textile reinforced thermoplastics. Composites A 2014;56:80–92. http://dx.doi.org/10.1016/j.compositesa.2013.09.009.

[20] Guzman-Maldonado E, Hamila N, Boisse P, Bikard J. Thermomechanical analysis, modelling and simulation of the forming of pre-impregnated thermoplastics composites. Composites A 2015;78:211–22. http://dx.doi.org/10.1016/j.compositesa.2015.08.017.

[21] Guzman-Maldonado E, Hamila N, Naouar N, Moulin G, Boisse P. Simulation of thermoplastic prepreg thermoforming based on a visco-hyperelastic model and a thermal homogenization. Mater Des 2016;93:431–42. http://dx.doi.org/10.1016/j.matdes.2015.12.166.

[22] Dörr D, Schirmaier FJ, Henning F, Kärger L. A viscoelastic approach for modeling bending behavior in finite element forming simulation of continuously fiber reinforced composites. Composites A 2017;94:113–23. http://dx.doi.org/10.1016/j.compositesa.2016.11.027.
[23] Werner HO, Dörr D, Henning F, Kärger L. Numerical modeling of a hybrid forming process for three-dimensionally curved fiber-metal laminates. AIP Conf Proc 2019;2113(1):020019. http://dx.doi.org/10.1063/1.5112524.
[24] Werner HO, Poppe C, Henning F, Kärger L. Material modeling in forming simulation of three-dimensional fiber-metal-laminates – A parametric study. Procedia Manuf 2020;47:154–61. http://dx.doi.org/10.1016/j.promfg.2020.04.160.
[25] Boisse P, Zouari B, Daniel J-L. Importance of in-plane shear rigidity in finite element analyses of woven fabric composite preforming. Composites A 2006;37(12):2201–12. http://dx.doi.org/10.1016/j.compositesa.2005.09.018.
[26] Jauffrès D, Morris CD, Sherwood JA, Chen J. Simulation of the thermostamping of woven composites: mesoscopic modelling using explicit fea codes. Int J Mater Form 2009;2(1):173–6. http://dx.doi.org/10.1007/s12289-009-0519-4.
[27] Jauffrès D, Sherwood JA, Morris CD, Chen J. Discrete mesoscopic modeling for the simulation of woven-fabric reinforcement forming. Int J Mater Form 2010;3(2):1205–16. http://dx.doi.org/10.1007/s12289-009-0646-y.
[28] Boisse P, Bai R, Colmars J, Hamila N, Liang B, Madeo A. The need to use generalized continuum mechanics to model 3D textile composite forming. Appl Compos Mater 2018;25(4):761–71. http://dx.doi.org/10.1007/s10443-018-9719-8.
[29] Aimène Y, Vidal-Sallé E, Hagège B, Sidoroff F, Boisse P. A hyperelastic approach for composite reinforcement large deformation analysis. J Compos Mater 2010;44(1):5–26. http://dx.doi.org/10.1177/0021998309345348.
[30] Kärger L, Galkin S, Dörr D, Poppe C. Capabilities of macroscopic forming simulation for large-scale forming processes of dry and impregnated textiles. Procedia Manuf 2020;47:140–7. http://dx.doi.org/10.1016/j.promfg.2020.04.155.
[31] Xue P, Peng X, Cao J. A non-orthogonal constitutive model for characterizing woven composites. Composites A 2003;(34):183–93.
[32] Peng XQ, Cao J. A continuum mechanics-based non-orthogonal constitutive model for woven composite fabrics. Composites A 2005;36(6):859–74. http://dx.doi.org/10.1016/j.compositesa.2004.08.008.
[33] Lee W, Cao J, Badel P, Boisse P. Non-orthogonal constitutive model for woven composites incorporating tensile effect on shear behavior. Int J Mater Form 2008;1(1):891–4. http://dx.doi.org/10.1007/s12289-008-0239-1.
[34] Lee W, Byun J, Um M, Cao J, Boisse P. Coupled non-orthogonal constitutive model for woven fabric composites. 2009, 17th International Conference on Composite Materials, ICCM-17 ; Conference date: 27-07-2009 Through 31-07-2009.
[35] Lee W, Cao J. Numerical simulations on double-dome forming of woven composites using the coupled non-orthogonal constitutive model. Int J Mater Form 2009;2(1):145–8. http://dx.doi.org/10.1007/s12289-009-0499-4.
[36] Peng X, Guo Z, Du T, Yu W-R. A simple anisotropic hyperelastic constitutive model for textile fabrics with application to forming simulation. Composites B 2013;52:275–81. http://dx.doi.org/10.1016/j.compositesb.2013.04.014.
[37] Yao Y, Huang X, Peng X, Gong Y. An anisotropic constitutive model with biaxial-tension coupling for woven composite reinforcements. In: AIP conference proceedings 1769. American Institute of Physics; 2016, http://dx.doi.org/10.1063/1.4963562.
[38] Yao Y, Youkun G, Peng X, Huang X. Modeling biaxial-tension coupling in woven fabric. In: Proceedings of the 21st international conference on composite materials. 2017, URL http://iccm-central.org/proceedings/iccm21proceedings/papers/3045.pdf.
[39] Yao Y, Huang X, Peng X, Liu P, Youkun G. An anisotropic hyperelastic constitutive model for plain weave fabric considering biaxial tension coupling. Text Res J 2019;89(3):434–44. http://dx.doi.org/10.1177/0040517517748495.
[40] Yao Y, Peng X, Gong Y. Influence of tension–shear coupling on draping of plain weave fabrics. J Mater Sci 2019;54(8):6310–22. http://dx.doi.org/10.1007/s10853-019-03334-w.
[41] Sargent J, Chen J, Sherwood J, Cao J, Boisse P, Willem A, Vanclooster K, Lomov SV, Khan M, Mabrouki T, Fetfatsidis K, Jauffrès D. Benchmark study of finite element models for simulating the thermostamping of woven-fabric reinforced composites. Int J Mater Form 2010;3(1):683–6. http://dx.doi.org/10.1007/s12289-010-0862-5.
[42] Allen MB. Continuum mechanics: the birthplace of mathematical models. Hoboken, New Jersey: Wiley; 2016.
[43] Spencer AJM. Continuum mechanics. Dover books on physics, Newburyport: Dover Publications; 2012, URL http://gbv.eblib.com/patron/FullRecord.aspx?p=1894359.
[44] Spencer AJM, editor. Continuum theory of the mechanics of fibre-reinforced composites. International centre for mechanical sciences, courses and lectures, vol. 282, Wien: Springer Vienna; 1984, http://dx.doi.org/10.1007/978-3-7091-4336-0.
[45] Hackett RM. Hyperelasticity primer. 2nd ed.. Cham: Springer International Publishing; 2018, http://dx.doi.org/10.1007/978-3-319-73201-5.
[46] Döbrich O, Gereke T, Diestel O, Krzywinski S, Cherif C. Decoupling the bending behavior and the membrane properties of finite shell elements for a correct description of the mechanical behavior of textiles with a laminate formulation. J Ind Text 2014;44(1):70–84. http://dx.doi.org/10.1177/1528083713477442.
[47] Hoess KM, Guski V, Keller F, Schmauder S. Experimental 3D characterization and parametrization of an anisotropic constitutive law for a synthetic nonwoven. J Text Inst 2021;1–10. http://dx.doi.org/10.1080/00405000.2021.1898738.
[48] Naujokaitytė L, Strazdienė E. Investigation of textile fabrics behavior under compression. Mater Sci (MedžIagotyra) 2007;13(4):337–42.
[49] Selezneva M, Naouar N, Denis Y, Gorbatikh L, Hine P, Lomov SV, Swolfs Y, Verpoest I, Boisse P. Identification and validation of a hyperelastic model for self-reinforced polypropylene draping. Int J Mater Form 2021;14(1):55–65. http://dx.doi.org/10.1007/s12289-020-01542-3.
[50] Komeili M. Multi-scale characterization and modeling of shear-tension interaction in woven fabrics for composite forming and structural applications (Ph.D. thesis), Okanagan: The University of British Columbia; 2014.
[51] Cherouat A, Bourouchaki H. Numerical tools for composite woven fabric preforming. Adv Mater Sci Eng 2013;2013(1):1–18. http://dx.doi.org/10.1155/2013/709495, URL https://www.researchgate.net/publication/258397186_Numerical_Tools_for_Composite_Woven_Fabric_Preforming.
[52] Mennecart T, Gies S, Ben Khalifa N, Tekkaya AE. Analysis of the influence of fibers on the formability of metal blanks in manufacturing processes for fiber metal laminates. J Manuf Mater Process 2019;3(1):2. http://dx.doi.org/10.3390/jmmp3010002.
[53] Lin H, Long AC, Sherburn M, Clifford MJ. Modelling of mechanical behaviour for woven fabrics under combined loading. Int J Mater Form 2008;1(1):899–902. http://dx.doi.org/10.1007/s12289-008-0241-7.
[54] Charmetant A, Orliac JG, Vidal-Sallé E, Boisse P. Hyperelastic model for large deformation analyses of 3D interlock composite preforms. Compos Sci Technol 2012;72(12):1352–60. http://dx.doi.org/10.1016/j.compscitech.2012.05.006.
[55] Pazmino J, Mathieu S, Carvelli V, Boisse P, Lomov SV. Numerical modelling of forming of a non-crimp 3D orthogonal weave E-glass composite reinforcement. Composites A 2015;72:207–18. http://dx.doi.org/10.1016/j.compositesa.2015.02.013.
[56] Boisse P, Colmars J, Hamila N, Naouar N, Steer Q. Bending and wrinkling of composite fiber preforms and prepregs. A review and new developments in the draping simulations. Composites B 2018;141:234–49. http://dx.doi.org/10.1016/j.compositesb.2017.12.061.
[57] Boisse P, Hamila N, Madeo A. The difficulties in modeling the mechanical behavior of textile composite reinforcements with standard continuum mechanics of Cauchy. Some possible remedies. Int J Solids Struct 2018;154:55–65. http://dx.doi.org/10.1016/j.ijsolstr.2016.12.019.
[58] Wang J, Wang P, Hamila N, Boisse P. Mesoscopic analyses of the draping of 3D woven composite reinforcements based on macroscopic simulations. Compos Struct 2020;250:112602. http://dx.doi.org/10.1016/j.compstruct.2020.112602.
[59] Boisse P, Huang J, Guzman-Maldonado E. Analysis and modeling of wrinkling in composite forming. J Compos Sci 2021;5(3):81. http://dx.doi.org/10.3390/jcs5030081.
[60] Poppe C, Dörr D, Henning F, Kärger L. Experimental and numerical investigation of the shear behaviour of infiltrated woven fabrics. Composites A 2018;114:327–37. http://dx.doi.org/10.1016/j.compositesa.2018.08.018.